Volume 27
Number 41
7 November 2025
Pages 21853–22290

PCCP

Physical Chemistry Chemical Physics

rsc.li/pccp

25 YEARS ANNIVERSARY

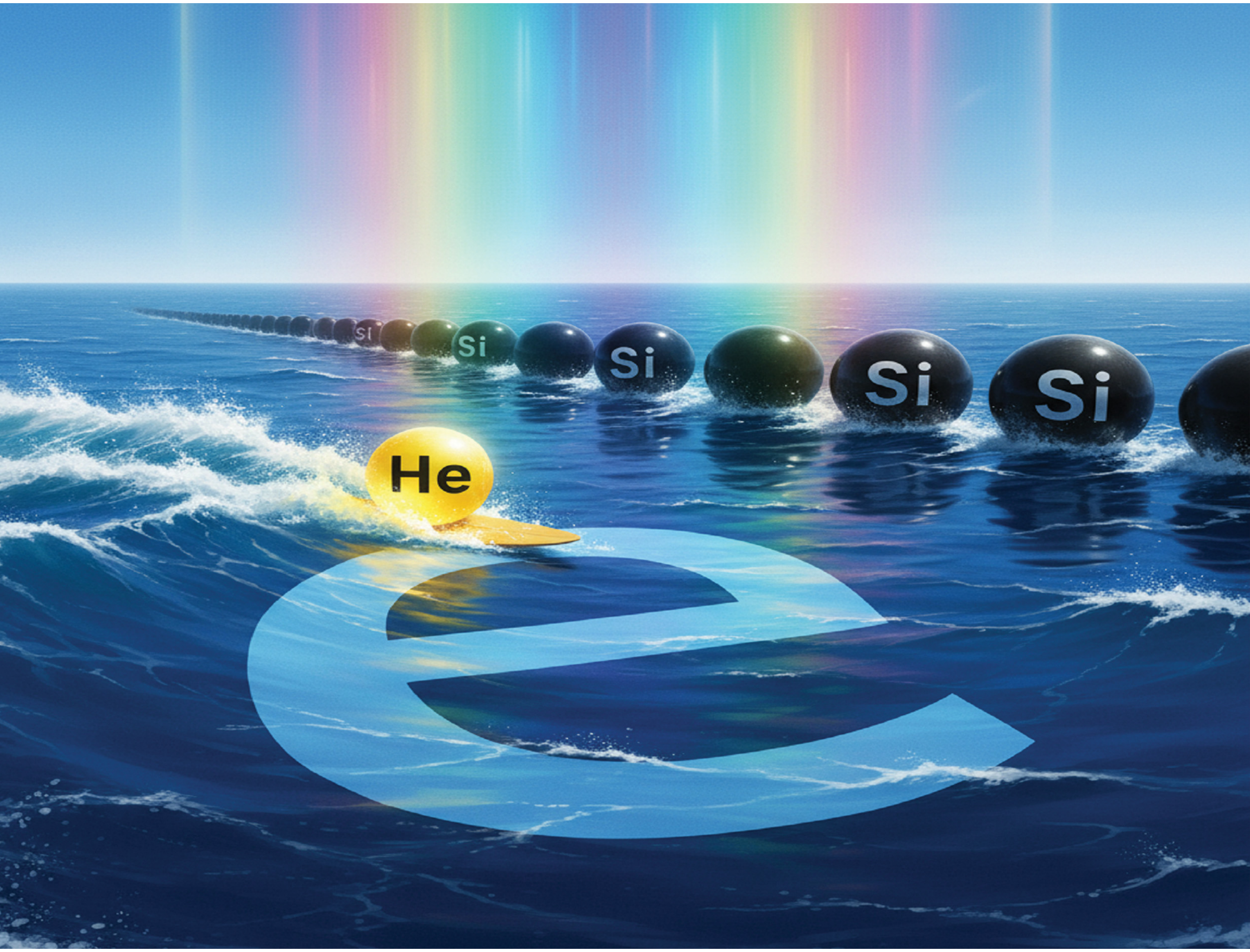

ISSN 1463-9076

ROYAL SOCIETY OF CHEMISTRY

PAPER
Feng Wang, Lan Jiang *et al.*
Electron stopping power of α-particles in silicon regulated by ultrashort pulse lasers

PCCP Owner Societies

PCCP

ROYAL SOCIETY OF CHEMISTRY

PAPER

View Article Online
View Journal | View Issue

Cite this: *Phys. Chem. Chem. Phys.*, 2025, **27**, 21878

Received 16th August 2025,
Accepted 15th September 2025

DOI: 10.1039/d5cp03149d

rsc.li/pccp

Electron stopping power of α-particles in silicon regulated by ultrashort pulse lasers

Ya-Ting Sun,†[a] Xiao-Ning Yang, †[a] Xin Shen,[b] Feng Wang *[a] and Lan Jiang *[c]

We conducted a study on the electron stopping power of α-particles in silicon crystals regulated by ultrashort pulse lasers, using time-dependent density functional theory non-adiabatically coupled with molecular dynamics. Our investigation focused on α-particles with initial velocities ranging from 0.1 to 1.0 a.u., providing detailed insights into the electronic states involved in the stopping process with exceptional spatial and temporal resolution. Our findings show how pulse lasers can influence electron stopping power and the degree to which this stopping power can be controlled by the laser pulses.

1 Introduction

When an incident particle traverses a material, it undergoes scattering at various angles and experiences a reduction in kinetic energy due to collisions with nuclei and electrons within the material.[1] Developing a comprehensive theoretical understanding of particle–matter interactions is crucial for addressing key challenges across numerous fields, including the nuclear industry,[2–4] space technology,[5] high-energy density physics,[6] medical radiotherapy,[7–9] fundamental research,[10] and integrated circuit fabrication.[11]

In general, a material's ability to slow down moving projectile particles is referred to as its stopping power.[12–15] Conceptually, the stopping power of a material against a specific projectile can be categorized into two types based on the particles that make up the material. The first is nuclear stopping power (S_n), which occurs at low projectile velocities and involves primarily energy transfer to nuclei without electronic excitations.[15,16] The second is electron stopping power (S_e), which becomes significant at higher projectile velocities, where the predominant energy transfer occurs to electrons.[16–19]

While the stopping power of materials in their ground state under ion irradiation has been extensively studied through both experimental[20–23] and theoretical[24–27] methods, comparatively less attention has been given to the stopping power of materials when they are in excited states. Currently, there is limited research on how the excited states of target electrons influence the stopping power of target materials for projectile ions. For instance, Pang *et al.*[28] performed a theoretical study analyzing the interaction of helium ions with aluminum targets at finite temperatures, employing time-dependent density functional theory (TDDFT) non-adiabatically coupled with molecular dynamics (TDDFT-MD).[29,30] Their results provide important understanding of how temperature affects stopping power in aluminum targets for temperatures below 500 K, indicating that electron temperature exerts minimal impact on S_e in this low-temperature regime. Furthermore, Sun *et al.*[31] investigated the S_e of protons in aluminum crystals at high electron temperatures using a quantum-blocking mechanism based on a physical picture of electronic transitions in energy levels for explaining the phenomenon of the S_e decreasing with the increase of target electron temperature. Interestingly, by manipulating ultrashort pulse lasers in either the time or spatial domain, it becomes possible to control photon–electron interactions within materials.[32,33] This capability, in turn, enables the regulation of the material's electronic states and ultimately results in changes to its properties. It appears that the capability to manipulate and control a material's properties with an ultrashort pulse laser offers a variety of fascinating applications.

Based on these achievements, our objective is to explore the effects of pulse lasers on S_e and the fundamental physical mechanisms involved. Specifically, we focus on the S_e of α-particles in silicon, modulated by ultrashort pulse lasers. We are motivated to carry out numerical simulations to understand how laser pulses control S_e and to what extent S_e can be controlled by these laser pulses.

The remainder of this paper is organized as follows. In Section 2, we describe the computational methodology and model employed to study the S_e of α-particles in silicon

---

[a] School of Physics, Beijing Institute of Technology, Beijing 100081, China. E-mail: wangfeng01@tsinghua.org.cn
[b] China Mobile (Hangzhou) Information Technology Co., Ltd., Hangzhou 310023, China
[c] Laser Micro/Nano-Fabrication Laboratory, School of Mechanical Engineering, Beijing Institute of Technology, Beijing 100081, China. E-mail: jianglan@bit.edu.cn

† These authors contributed equally to this work.

regulated by ultrashort pulse lasers. Section 3 presents a detailed analysis of the simulation results, including explanations of the observed phenomena. Finally, Section 4 summarizes the key conclusions derived from this work.

2 Model and computational details

The S_e of α-particles in a silicon crystal was investigated using TDDFT-MD. In this collision system, particles are classified into two distinct categories: (i) ionic cores (nuclei with inner electrons), treated as classical point charges with coordinates $\mathbf{R}_j$ ($j = 1, \ldots, N_{\text{ion}}$), and (ii) valence electrons, described by single-particle wavefunctions ψ_i ($i = 1, \ldots, N_e$). The electron dynamics are governed by the time-dependent Kohn–Sham (TDKS) equation (atomic units are used unless stated otherwise):

$$i\hbar\frac{\partial\psi_i(\mathbf{r},t)}{\partial t} = \hat{H}_{\text{KS}}(\mathbf{r},t)\psi_i(\mathbf{r},t), \tag{1}$$

where the Hamiltonian $\hat{H}_{\text{KS}}$ is defined as:

$$\hat{H}_{\text{KS}}(\mathbf{r},t) = \frac{1}{2m_e}\left(-i\hbar\nabla + \frac{e}{c}\mathbf{A}(t)\right)^2 + V_{\text{KS}}(\mathbf{r},t), \tag{2}$$

where m_e is the electron mass, c is the speed of light in vacuum, and e ($e > 0$) is the elementary charge. The TDKS potential V_{KS} consists of three components:

$$V_{\text{KS}}(\mathbf{r},t) = V_{\text{en}}(\mathbf{r},\mathbf{R}(t)) + V_{\text{H}}[\rho](\mathbf{r},t) + V_{\text{XC}}[\rho](\mathbf{r},t), \tag{3}$$

where V_{en} represents the electron–nucleus interaction potential, using either pseudopotential or all-electron approaches, V_{H} describes the Hartree potential accounting for electron–electron Coulomb repulsion, and V_{XC} is the exchange–correlation (XC) potential. The electron density ρ is expressed as

$$\rho(\mathbf{r},t) = \sum_{i=1}^{M} f_i|\psi_i(\mathbf{r},t)|^2, \tag{4}$$

where f_i denotes the occupation number of the ith Kohn–Sham (KS) orbital. The occupation number satisfy

$$\sum_{i=1}^{M} f_i = N_e, \tag{5}$$

with N_e representing the total number of electrons.

Within the framework of density functional theory (DFT)[34,35] and TDDFT, the standard approach is to fully occupy all KS orbitals with energies below the Fermi level, while orbitals above this level remain unoccupied. Before starting the time evolution calculation, the ground state electronic structure is computed by solving the static KS equation $\hat{H}_{\text{KS}}(0)\psi_i(0) = \varepsilon_i(0)\psi_i(0)$, where $\hat{H}_{\text{KS}}(0)$ is the KS Hamiltonian at the initial time, and $\varepsilon_i(0)$ and $\psi_i(0)$ are the corresponding eigenvalues and eigenstates. These ground state orbitals $\psi_i(0)$ serve as the starting point for the subsequent time-dependent evolution. During evolution, the instantaneous single-particle orbital energy $\varepsilon_i(t)$ at time t satisfy: $\varepsilon_i(t) = \langle\psi_i(\mathbf{r},t)|\hat{H}_{\text{KS}}(t)|\psi_i(\mathbf{r},t)\rangle$.

The laser field is described through the time-dependent vector potential **A**:

$$\mathbf{A}(t) = -\frac{\mathbf{E_0}}{\omega}\cos^2\left(\frac{\pi t}{T}\right)\sin(\omega t), \quad \left(-\frac{T}{2} < t < \frac{T}{2}\right), \tag{6}$$

where $\mathbf{E_0}$ is the amplitude with the pulse polarization direction oriented along x-axis, ω is the angular frequency, and T denotes the total pulse duration. The corresponding electric field is given by:

$$\mathbf{E}(t) = -\frac{1}{c}\frac{\mathrm{d}\mathbf{A}(t)}{\mathrm{d}t}. \tag{7}$$

Meanwhile, the ionic core motion follows the classical Newton equation:

$$M_j\frac{\mathrm{d}^2\mathbf{R}_j(t)}{\mathrm{d}t^2} = \mathbf{F}_j(t), \tag{8}$$

where M_j is the mass of the jth ionic core, and $\mathbf{F}_j$ is the force acting on the jth ionic core, which can be expressed as:

$$\mathbf{F}_j = -\nabla_{\mathbf{R}_j}\left[\sum_{j\neq k}\frac{Z_jZ_k e^2}{|\mathbf{R}_j - \mathbf{R}_k|} + \sum_{i=1}^{M} f_i\langle\psi_i|\hat{H}_{\text{KS}}|\psi_i\rangle\right], \tag{9}$$

where Z_j is the charge of the jth ionic core.

In this study, the pulse laser width was set to 2 fs, the wavelength to 800 nm ($\hbar\omega$ = 1.55 eV), and the intensity ranged from $I = 1 \times 10^{11}$ W cm^{-2} to $I = 1 \times 10^{15}$ W cm^{-2}, with propagation along the z-axis and polarization oriented along the x-axis. This configuration was chosen because ultrashort pulse lasers can induce profound, damage-free modifications in the electric and optical properties of dielectric materials, thereby enabling precise control of electron dynamics at the atomic scale.[36,37]

Based on the conventional cubic unit cell of silicon[38] ($a = b = c = 5.467$ Å; Fig. 1(a)), we constructed a supercell with periodic boundary conditions. Cleaving this supercell along the (111) plane yielded a new supercell (10.8614 Å × 11.5203 Å × 15.3603 Å; Fig. 1(b)). Electronic structure calculations employ Troullier–Martins norm-conserving pseudopotentials for silicon (with core configuration $1s^22s^22p^6$) and helium, implemented within the local density approximation (LDA)[39] to account for XC effects. A 2 × 2 × 2 Monkhorst–Pack k-point grid is used to sample the Brillouin zone. A real-space mesh spacing of 0.4 a.u., corresponding to a plane-wave energy cutoff of 52.06 Ry, ensures accurate unitary time propagation. The propagation step length, $\Delta t \times \nu \sim 3.9 \times 10^{-3}$ Å,[17,40] is adopted for various α-particle velocities to guarantee energy convergence of the time-dependent evolution with 800 empty states included. To numerically integrate the equations of motion, the velocity Verlet algorithm is employed for ionic cores, and an enforced time-reversal symmetry algorithm[41] is used for the TDKS equations.

During real-time simulations, α-particles initially positioned at the left boundary of the simulation box move along the positive z-axis with velocity ν (see Fig. 1(b)). To elucidate the variation trend of S_e in lattice channeling and off-channeling regions, three impact parameter cases (*i.e.*, the closest

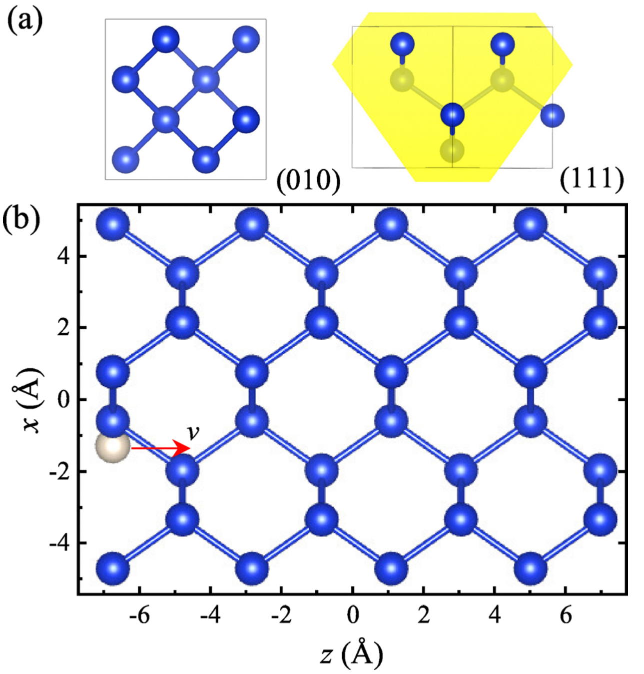

Fig. 1 (a) Silicon unit cell structure (left) and atomic arrangement in the (111) plane (right). (b) Schematic of the initial simulation setup at time $t = 0$. Gray and blue spheres represent the α-particle and silicon nuclei, respectively. The α-particle is initially positioned at $z_0 = -7.68$ Å and moves along the positive z-axis toward $z = 7.68$ Å with velocity v.

approach distance between incident particles and target atoms) were selected for comparative analysis. As illustrated in the inset of Fig. 3, these positions are determined based on the geometric features of the hexagonal lattice structure: the center of the silicon atom hexagon is defined as the channeling region (channel-1), the intermediate position at half the bond length perpendicular to the adjacent Si–Si bond is designated as channel-2, and the midpoint of the Si–Si bond is defined as the off-channeling region (channel-3).

All calculations were performed using Octopus code.[42,43] Specifically, the calculation steps are divided into the following three steps: first, obtain a silicon crystal in the electronic ground state using DFT calculation. Then, TDDFT is used to simulate the dynamic evolution process of electrons in silicon crystals under the action of ultrashort laser pulses. Finally, TDDFT-MD is used to simulate α-particles passing through silicon crystals irradiated by ultrashort laser pulses.

3 Results and discussion

Fig. 2 illustrates the variation of the kinetic energy loss ΔE_k as a function of the displacement of an α-particle through a silicon crystal, along both channel-1 and channel-3 trajectories. The abrupt initial motion of the projectiles at the start of the time-dependent evolution introduces an artificial disturbance in the kinetic energy loss. To minimize the impact of this artifact, the S_e is evaluated by time-averaging the instantaneous S_e, defined as $S_e(v) = -\dfrac{dE_k}{dz}$, over two lattice periods, which is indicated by the vertical dashed lines in Fig. 2. As the displacement increases, the kinetic energy loss of α-particles with various velocities shows a gradually increasing trend with different slopes. The periodic oscillations observed in the kinetic energy loss reflect the crystal lattice structure of silicon. Notably, these oscillations are more pronounced when the α-particles travel along the channel-3 trajectory.

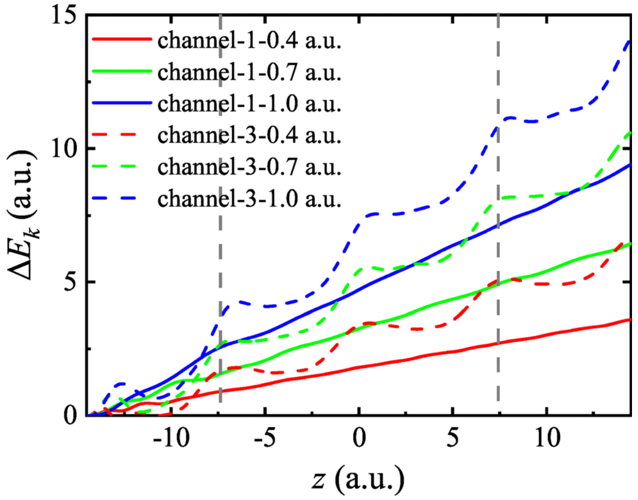

Fig. 2 The kinetic energy loss $\Delta E_k = E_k(z_0) - E_k(z)$ of the α-particle as a function of displacement along the z-axis for channel-1 (solid line) and channel-3 (dashed line) trajectories.

Fig. 3 compares the S_e calculated from TDDFT-MD simulations with experimental data[44–46] and SRIM-2013 predictions (for silicon with density 2.3212 g cm^{-3}).[48] The TDDFT-MD results show higher S_e values than SRIM-2013, but are in good agreement with the experimental data of Tran *et al.*[44] and

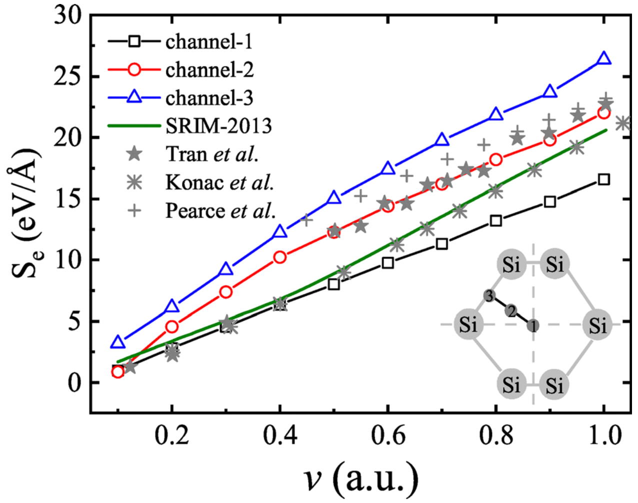

Fig. 3 The S_e of silicon crystal against an α-particle moving is represented as a function of velocity. The symbols denote the calculated values along different channels: ☐ for channel-1, ○ for channel-2, and △ for channel-3 trajectories. Experimental data are represented by ★ (Tran *et al.*[44]), * (Konac *et al.*[45]), and + (Pearce *et al.*[46]). The green curve corresponds to SRIM-2013 predictions.[47] The inset shows a top view of the channel geometry.

Pearce *et al.*,[46] thereby validating the computational methods and silicon structural models used in this study. Experimental measurements typically involve averaging over trajectories in amorphous or polycrystalline targets, which diminishes channeling effects. SRIM-2013 accounts for this through averaging over impact parameters. TDDFT-MD simulations explicitly model the periodic crystalline environment, thereby enhancing channeling effects along specific trajectories (*e.g.*, axial or planar channels). Several interesting findings are as follows: (i) velocity dependence: S_e increases monotonically with α-particle velocity for all trajectories. (ii) Trajectory sensitivity: the influence of the trajectory becomes more pronounced at higher velocities.

As Fig. 3 shows, three different incident trajectories were calculated, and the trend of S_e variation with α-particle velocity remains consistent across all channels. Based on this observation, channel-1 is selected as a representative trajectory for in-depth analysis to effectively illustrate the effect of laser irradiation on the S_e of silicon crystals. Fig. 4 depicts the ΔE_k of α-particle traveling along channel-1 at a velocity of 1.0 a.u. in silicon crystals after irradiation with different laser intensities is a function of displacement along the *z*-axis. Several interesting findings are as follows: (i) for silicon crystals irradiated with high laser intensity ($I > 1 \times 10^{14}$ W cm^{-2}), the ΔE_k of the α-particle is markedly lower than in unirradiated crystals. (ii) For silicon crystals irradiated with low to medium laser intensities ($I \leq 1 \times 10^{14}$ W cm^{-2}), the ΔE_k is slightly increased relative to unirradiated crystals (see inset of Fig. 4). (iii) The ΔE_k first increases and then decreases as the laser intensity rises.

To further clarify the effect of laser irradiation on the S_e of crystals, Fig. 5 shows the variation of S_e with laser intensity at three different α-particle velocities. Several interesting findings are as follows: (i) S_e initially increases and then decreases with increasing laser intensity. (ii) The effect of laser intensity on S_e is significantly stronger for faster α-particles (*e.g.*, v = 1.0 a.u.) than for slower ones (*e.g.*, v = 0.4 a.u.). (iii) Notably, the peak value of S_e occurs at the same laser intensity of $I = 1 \times 10^{14}$ W cm^{-2} for all three velocities investigated.

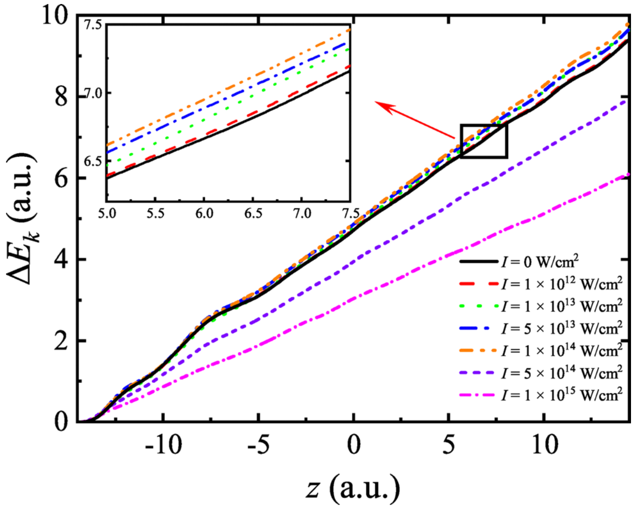

Fig. 4 The kinetic energy loss $\Delta E_k = E_k(z_0) - E_k(z)$ of α-particle traveling along channel-1 at a velocity of 1.0 a.u. in silicon crystals after irradiation with different laser intensities is a function of displacement along the *z*-axis.

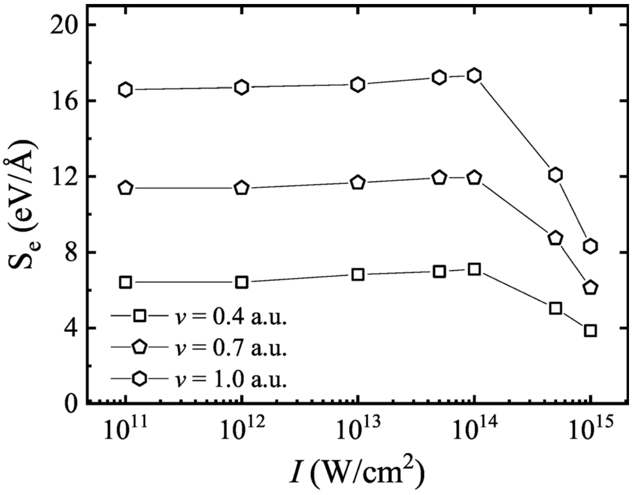

Fig. 5 The S_e of silicon crystal against an α-particle at different velocities along channel-1 moving is represented as a function of laser intensity.

To understand this non-monotonic dependence of S_e on laser intensity, we consider two competing effects induced by the laser field. First, increasing the laser intensity can raise the concentration of free electrons in silicon, which enhances the collision probability between free electrons and incident particles. This mechanism can increase the S_e. Second, increasing the laser intensity can enhance electronic excitation, leading to a reduction in S_e through a quantum-blocking mechanism as follows: (i) the S_e in silicon crystal originates from electron transitions between occupied and unoccupied states induced by the incident particles. (ii) The transition probability from low-energy occupied states to high-energy unoccupied states is higher than that from high-energy occupied states to even higher-energy empty states. (iii) At low electronic excitation, electrons mainly occupy low-energy states, leaving higher-energy states mostly empty, which facilitates electron transitions induced by incident particles. (iv) Conversely, at high electronic excitation, electrons occupying higher-energy states can block electron transitions induced by incident particles, leading to a reduction in S_e.

Next, to validate the proposed electronic excitation mechanism, we introduce the occupation distribution function defined as

$$f(\varepsilon, t) = \sum_{i,j} f_j \left| \left\langle \psi_i(0) \middle| \psi_j(t) \right\rangle \right|^2 L(\varepsilon - \varepsilon_i(0)), \tag{10}$$

where L is a normalized Gaussian lineshape function centered at $\varepsilon_i(0)$, expressed as

$$L(\varepsilon - \varepsilon_i(0)) = \frac{1}{\sqrt{\pi}\sigma} \exp\left(-\frac{(\varepsilon - \varepsilon_i(0))^2}{\sigma^2} \right), \tag{11}$$

where σ defines the spectral broadening width of the Gaussian.

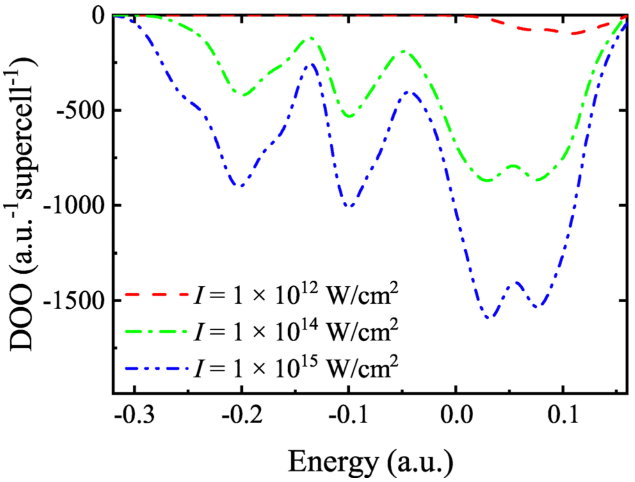

Fig. 6 Differences of occupancy distribution functions below the Fermi level of silicon crystals before and after laser irradiation with different intensities. The Fermi energy is at 0.16 a.u.

The difference of occupation distribution function (DOO) before ($t = t_1$) and after ($t = t_2$) the interaction is defined as is defined as

$$\mathrm{DOO}(\varepsilon,t_1,t_2) = f(\varepsilon,t_2) - f(\varepsilon,t_1). \tag{12}$$

Fig. 6 shows the DOO below the Fermi level of silicon crystals before and after laser irradiation with different intensities. The valley in the DOO signifies electron excitation, and its integrated area is the number of excited electrons. It can be seen that several valleys appeared, indicating significant electron excitation into the conduction band. Obviously, laser irradiation promotes electron excitation in the silicon crystal, with the number of excited electrons rising as the laser intensity increases. Moreover, electrons bound in deeper energy levels of a silicon crystal have been excited into the conduction band by more intense laser irradiation, contributing to an increase in the concentration of free electrons.

Fig. 7 shows the DOO below the Fermi level before and after α-particle collisions at different velocities along channel-1 within a silicon crystal, subsequent to irradiation by lasers of varying intensities. The solid line represents the case without laser irradiation for comparison. It can be observed that as the velocity of α-particles increases, fewer electrons are excited from shallow energy levels below the Fermi level to the conduction band, while more electrons are excited from deep energy levels below the Fermi level to the conduction band. From the perspective of photons, when projectile particles pass through silicon crystal, a changing electric field is created that includes virtual photons, leading to the generation of the DOO spectrum. Ref. 28 has demonstrated that higher-velocity projectiles carry more high-frequency photons, making them more likely to excite electrons bound in deeper energy levels.

To further verify the influence of laser irradiation on electron excitation in silicon crystals, Fig. 8 shows two-dimensional snapshots of the electron density distribution along the (010) and (111) planes under varying laser intensities. Without laser irradiation (I = 0 W cm^{-2}), the electron density exhibits clear covalent-bond characteristics. As the laser intensity increases to 1 × 10^{12} W cm^{-2}, minor changes in electron density distribution appear, while the overall bond structure remains largely intact. Upon further increasing the intensity to 1 × 10^{14} W cm^{-2}, the electron density shows noticeable diffusion, accompanied by a reduction in the covalent-bond characteristics and increased metal-bond characteristics. At a higher laser intensity of 1 × 10^{15} W cm^{-2}, the electron density becomes more dispersed and the covalent-bond characteristics are significantly diminished, suggesting severe disruption of the bond structure, potentially leading to metal-bonds or plasmonic behavior.

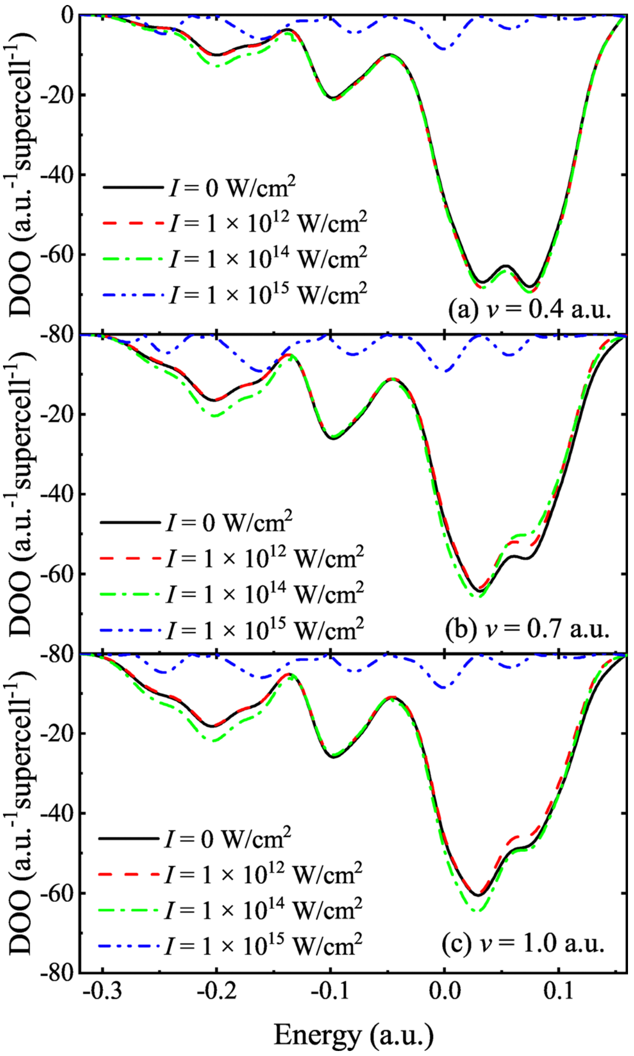

Fig. 7 Differences of occupancy distribution functions below the Fermi level before and after α-particle collisions at different velocities along channel-1 within a silicon crystal, subsequent to irradiation by lasers of varying intensities. The Fermi energy is at 0.16 a.u. (a) v = 0.4 a.u., (b) v = 0.7 a.u., (c) v = 1.0 a.u.

It is well established that during interactions between α-particles and target materials, the generation of electron–hole pairs due to electronic excitations introduces additional energy loss channels.[49] Fig. 9 presents the electron density difference in the system before and after the incident of

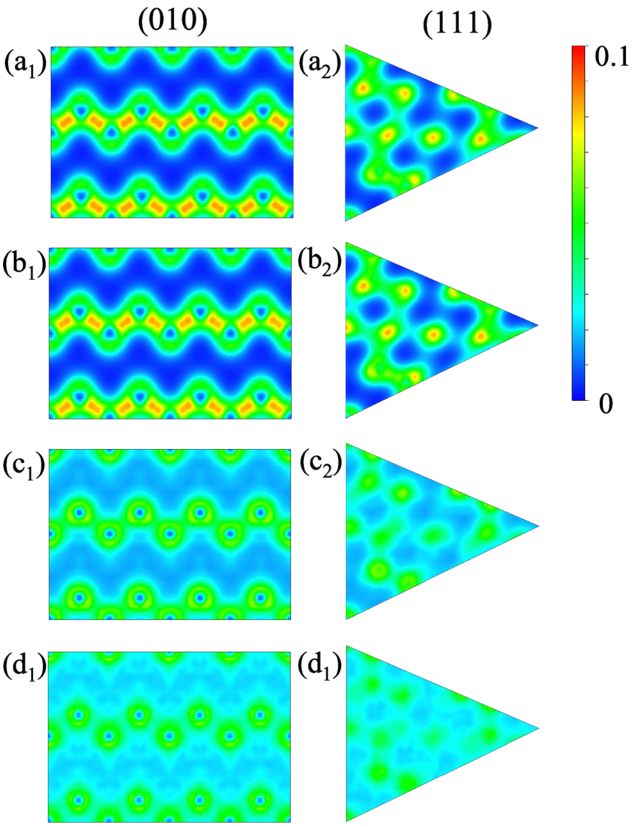

Fig. 8 Two-dimensional snapshots of the electron density distributions of the silicon crystal along the (010) (a_1)–(d_1) and (111) (a_2)–(d_2) planes after laser irradiation. Panels correspond to laser intensities: (a_1) and (a_2) I = 0 W cm^{-2}, (b_1) and (b_2) $I = 1 \times 10^{12}$ W cm^{-2}, (c_1) and (c_2) $I = 1 \times 10^{14}$ W cm^{-2}, and (d_1) and (d_2) $I = 1 \times 10^{15}$ W cm^{-2}.

α-particles moving along silicon crystal channel-1 at a velocity of 1.0 a.u., subsequent to irradiation by lasers of varying intensities. Several interesting findings are as follows: (1) as the laser intensity increases, the spatial distribution of electron–hole pairs excited by α-particles becomes less localized, indicating that laser can regulate the spatial range of the interaction between α-particles and electrons in silicon crystals. (2) For the laser intensity of $I = 1 \times 10^{14}$ W cm^{-2}, the number of electron–hole pairs generated by α-particle excitation appears to reach its maximum, implying the highest energy transfer between α-particles and silicon crystals, consistent with the position of the S_e peak shown in Fig. 5.

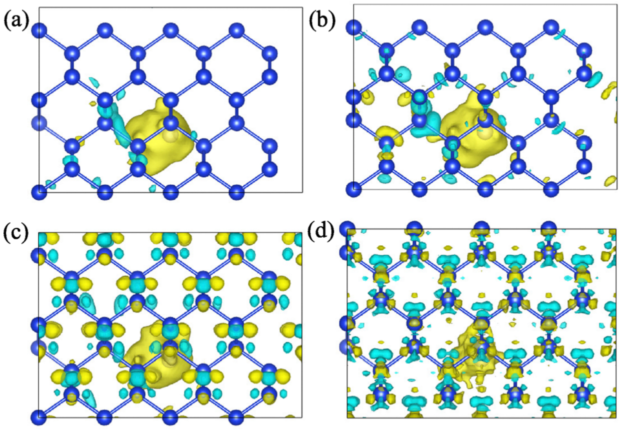

Fig. 9 Snapshot of the electron density difference in the system before and after the incident of α-particles moving along silicon crystal channel-1 at a velocity of 1.0 a.u., subsequent to irradiation by lasers of varying intensities. (a) I = 0 W cm^{-2}, (b) $I = 1 \times 10^{12}$ W cm^{-2}, (c) $I = 1 \times 10^{14}$ W cm^{-2}, and (d) $I = 1 \times 10^{15}$ W cm^{-2}. Yellow and blue regions indicate positive and negative values of the density difference, respectively.

The interaction between ultrashort laser pulses and matter is highly dependent on laser parameters and material intrinsic properties. As shown in Fig. 10(a), after laser irradiation of silicon crystals, the average number of excited electrons (n_e) per silicon atom significantly increases with the increase of laser intensity, which is a mechanism causing S_e to increase with the increase of laser intensity. To quantitatively characterize the degree of electron excitation, we define the sum of single-particle orbital energy (E_{eig}) as follows:

$$E_{\text{eig}} = \sum_{i}^{N_e} \varepsilon_i(t). \tag{13}$$

A higher/lower E_{eig} value indicates that the electron is in a higher/lower excitation state. Fig. 10(b) shows that E_{eig} increases with increasing laser intensity, further confirming that electron are excited to higher-energy states with increasing laser intensity, which is another mechanism causing S_e to decrease with the increase of laser intensity. The increase of laser intensity leads to competition between these two

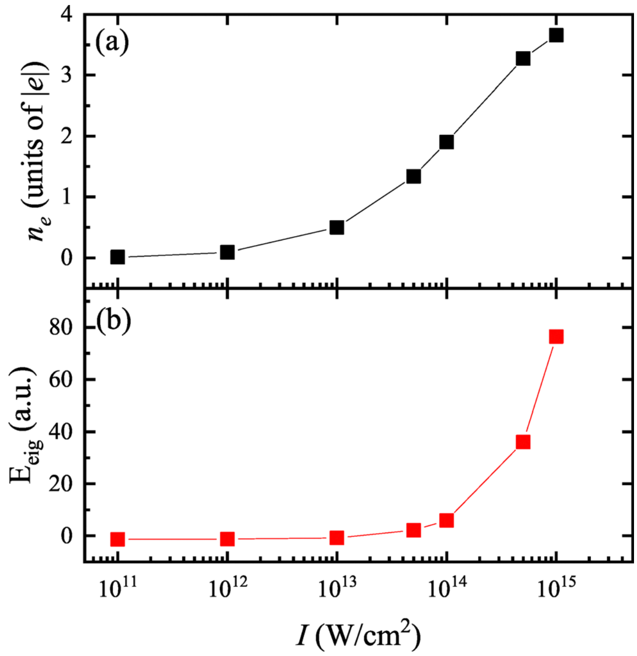

Fig. 10 (a) The average number of excited electrons (n_e) per silicon atom after laser irradiation of a silicon crystal as a function of laser intensity. (b) The sum of single-particle orbital energy (E_{eig}) of the system after laser irradiation of silicon crystals is represented as a function of laser intensity.

mechanisms, ultimately resulting in the peak phenomenon of S_e as a function of laser intensity shown in Fig. 5.

4 Conclusions

In summary, a study was conducted on the electron stopping power of α-particles in silicon regulated by ultrashort pulse lasers, employing time-dependent density functional theory coupled nonadiabatically with molecular dynamics. This method provided detailed insights into the electronic states involved in the stopping process with high spatial and temporal resolution, surpassing the capabilities of experimental tabulated data and leading to a range of intriguing findings: the ultrashort pulse laser can significantly regulate S_e. The effect of laser intensity on S_e becomes more pronounced as the projectile velocity increases. Additionally, the impact of laser intensity on S_e is more noticeable for high-velocity projectiles compared to low-velocity ones. After laser irradiation of silicon crystals, the average number of excited electrons significantly increases with the increase of laser intensity, which is a mechanism causing S_e to increase with the increase of laser intensity. The degree of electrons excition significantly increases with the increase of laser intensity, which is another mechanism causing S_e to decrease with the increase of laser intensity. The combination and mutual competition of both these two mechanisms, ultimately result in the peak phenomenon of S_e as a function of laser intensity.

While the S_e of materials in their ground state under ion irradiation has been extensively explored through both experimental techniques and theoretical modeling, comparatively less research has focused on the S_e of materials in excited electronic states. The ability to induce and precisely control localized transient electron states within materials using ultrashort pulse lasers offers a promising and innovative approach to modifying S_e. This method allows for the intentional alteration of materials away from their conventional ground states, potentially enabling controlled changes in their S_e properties. Exploring this phenomenon opens new avenues for scientific research and technological advancements, deserving to be investigated in future research both theoretically and experimentally.

Author contributions

Ya-Ting Sun: conceptualization (lead); data curation (equal); formal analysis (equal); methodology (equal); software (equal); visualization (lead); writing – original draft (lead); writing – review & editing (equal). Xiao-Ning Yang: data curation (equal); formal analysis (equal); methodology (equal); software (equal); writing – review & editing (equal). Xin Shen: conceptualization (supporting); data curation (supporting). Feng Wang: data curation (supporting); formal analysis (supporting); methodology (supporting); project administration (lead); resources (lead); writing – review & editing (equal). Lan Jiang: conceptualization (supporting); data curation (supporting); formal analysis (supporting); methodology (supporting).

Conflicts of interest

There are no conflicts to declare.

Data availability

The data supporting the results of this study can be obtained from the corresponding author. The code for OCTOPUS can be found at **https://gitlab.com/octopus-code/octopus**. The version of the code employed for this study is version 12.0.

Acknowledgements

This research was funded by the Beijing Natural Science Foundation of China under grant no. 1242026.

Notes and references

1 M. T. Robinson, *Philos. Mag.*, 1965, **12**, 741–765.
2 S. J. Zinkle and L. L. Snead, *Scr. Mater.*, 2018, **143**, 154–160.
3 G. Odette and B. D. Wirth, *Handbook of Materials Modeling*, Springer, Cham, 2005, pp. 999–1037.
4 F. F. Komarov, A. F. Komarov, V. V. Pil'ko and V. V. Pil'ko, *J. Eng. Phys. Thermophys.*, 2013, **86**, 1481–1484.
5 M. Yamaguchi, *Sol. Energy Mater. Sol. Cells*, 2001, **68**, 31–53.
6 P. K. Patel, A. J. Mackinnon, M. H. Key, T. E. Cowan, M. E. Foord, M. Allen, D. F. Price, H. Ruhl, P. T. Springer and R. Stephens, *Phys. Rev. Lett.*, 2003, **91**, 125004.
7 L. K. Mansur, *J. Nucl. Mater.*, 1994, **216**, 97–123.
8 D. Schardt, T. Elsässer and D. Schulz-Ertner, *Rev. Mod. Phys.*, 2010, **82**, 383–425.
9 M. Durante and J. S. Loeffler, *Nat. Rev. Clin. Oncol.*, 2010, **7**, 37–43.
10 S. J. Zinkle and B. N. Singh, *J. Nucl. Mater.*, 1993, **199**, 173–191.
11 R. Dong, H. Lu, C. Yang, Y. Zhang, R. Yao, Y. Wang and Y. A. Zhang, *Micromachines*, 2024, **15**, 541.
12 J. M. Pruneda, D. Sánchez-Portal, A. Arnau, J. I. Juaristi and E. Artacho, *Phys. Rev. Lett.*, 2007, **99**, 235501.
13 V. U. Nazarov, J. M. Pitarke, C. S. Kim and Y. Takada, *Phys. Rev. B:Condens. Matter Mater. Phys.*, 2005, **71**, 121106.
14 S. Lohmann and D. Primetzhofer, *Phys. Rev. Lett.*, 2020, **124**, 096601.
15 S. Lohmann, R. Holeňák and D. Primetzhofer, *Phys. Rev. A*, 2020, **102**, 062803.
16 A. A. Correa, J. Kohanoff, E. Artacho, D. Sánchez-Portal and A. Caro, *Phys. Rev. Lett.*, 2012, **108**, 213201.
17 S.-M. Li, F. Mao, X.-D. Zhao, B.-S. Li, W.-Q. Jin, W.-Q. Zuo, F. Wang and F.-S. Zhang, *Phys. Rev. B*, 2021, **104**, 214104.
18 C. Lan, J. M. Xue, Y. Zhang, J. R. Morris, Z. Zhu, Y. Gao, Y. G. Wang, S. Yan and W. J. Weber, *Nucl. Instrum. Methods Phys. Res., Sect. B*, 2012, **286**, 45–50.

19 R. Ullah, E. Artacho and A. A. Correa, *Phys. Rev. Lett.*, 2018, **121**, 116401.
20 D. Primetzhofer, *Phys. Rev. A:At., Mol., Opt. Phys.*, 2014, **89**, 032711.
21 S. P. Møller, A. Csete, T. Ichioka, H. Knudsen, U. I. Uggerhøj and H. H. Andersen, *Phys. Rev. Lett.*, 2004, **93**, 042502.
22 D. Primetzhofer, S. Rund, D. Roth, D. Goebl and P. Bauer, *Phys. Rev. Lett.*, 2011, **107**, 163201.
23 R. A. Wilhelm, E. Gruber, R. Ritter, R. Heller, S. Facsko and F. Aumayr, *Phys. Rev. Lett.*, 2014, **112**, 153201.
24 X. Qi, F. Bruneval and I. Maliyov, *Phys. Rev. Lett.*, 2022, **128**, 043401.
25 G. Massillon-JL, A. A. Correa, X. Andrade and E. Artacho, *Phys. Rev. Lett.*, 2025, **134**, 076401.
26 J. Halliday and E. Artacho, *Phys. Rev. B*, 2019, **100**, 104112.
27 A. Schleife, Y. Kanai and A. A. Correa, *Phys. Rev. B:Condens. Matter Mater. Phys.*, 2015, **91**, 014306.
28 S.-N. Pang, F. Wang, Y.-T. Sun, F. Mao and X.-L. Wang, *Phys. Rev. A*, 2022, **105**, 032803.
29 J. L. Alonso, X. Andrade, P. Echenique, F. Falceto, D. Prada-Gracia and A. Rubio, *Phys. Rev. Lett.*, 2008, **101**, 096403.
30 A. Castro, M. Isla, J. I. Martínez and J. Alonso, *Chem. Phys.*, 2012, **399**, 130–134.
31 Y.-T. Sun, F. Wang, F. Mao and C.-Z. Gao, *Phys. Rev. B*, 2025, **111**, 144303.
32 J. P. Colombier, P. Combis, A. Rosenfeld, I. V. Hertel, E. Audouard and R. Stoian, *Phys. Rev. B:Condens. Matter Mater. Phys.*, 2006, **74**, 224106.
33 L. Jiang, A.-D. Wang, B. Li, T.-H. Cui and Y.-F. Lu, *Light: Sci. Appl.*, 2018, **7**, 17134.
34 W. Kohn and L. J. Sham, *Phys. Rev.*, 1965, **140**, A1133–A1138.
35 P. Hohenberg and W. Kohn, *Phys. Rev.*, 1964, **136**, B864–B871.
36 X. Zhang, F. Wang, L. Jiang and Y. Yao, *Phys. Rev. B*, 2017, **95**, 184301.
37 X. Zhang, F. Wang, F. Zhang and Y. Yao, *Phys. Rev. B*, 2018, **97**, 014310.
38 Web site of ‘‘primitive cell structure’’, **https://aflowlib.org/search/**.
39 J. P. Perdew and A. Zunger, *Phys. Rev. B:Condens. Matter Mater. Phys.*, 1981, **23**, 5048–5079.
40 S.-M. Li, F. Mao, X.-D. Zhao, W.-Q. Jin, W.-Q. Zuo, B.-S. Li, F. Wang and F.-S. Zhang, *Phys. Rev. B*, 2022, **106**, 014103.
41 A. Castro, M. A. L. Marques and A. Rubio, *J. Chem. Phys.*, 2004, **121**, 3425–3433.
42 M. A. Marques, A. Castro, G. F. Bertsch and A. Rubio, *Comput. Phys. Commun.*, 2003, **151**, 60–78.
43 A. Castro, H. Appel, M. Oliveira, C. A. Rozzi, X. Andrade, F. Lorenzen, M. A. L. Marques, E. K. U. Gross and A. Rubio, *Phys. Status Solidi B*, 2006, **243**, 2465–2488.
44 T. T. Tran, L. Jablonka, B. Bruckner, S. Rund, D. Roth, M. A. Sortica, P. Bauer, Z. Zhang and D. Primetzhofer, *Phys. Rev. A*, 2019, **100**, 032705.
45 G. Konac, S. Kalbitzer, C. Klatt, D. Niemann and R. Stoll, *Nucl. Instrum. Methods Phys. Res., Sect. B*, 1998, 136–138.
46 J. D. Pearce and R. R. Hart, *J. Appl. Phys.*, 1981, **52**, 5056–5065.
47 *Web site of ‘‘SRIM-2013’’*, **https://www.srim.org/**.
48 J. F. Ziegler, J. P. Biersack and M. D. Ziegler, *The Stopping and Range of Ions in Matter*, Ion Implantation Press, 2008.
49 C.-K. Li, F. Wang, B. Liao, X.-P. OuYang and F.-S. Zhang, *Phys. Rev. B*, 2017, **96**, 094301.